
A FLEXIBLE WRAPPED LINDLEY-TYPE DISTRIBUTION FOR ANGULAR DATA MODELLING

Johan Ferreira

School of Statistics and Actuarial Science, University of the Witwatersrand, South Africa
johan.ferreira@wits.ac.za

Delene van Wyk-de Ridder

Department of Statistical Sciences, University of Cape Town, South Africa
Department of Statistics, University of Pretoria, South Africa
delene.vanwyk@uct.ac.za

Janet van Niekerk

Department of Statistics, University of Pretoria, South Africa
janet.vanniekerk@up.ac.za

March 18, 2026

ABSTRACT

Flexible distributions for modelling angular data have received considerable attention in recent years, with ongoing work extending existing circular models to provide greater flexibility in capturing diverse angular behaviours. In this paper, we introduce and study the w3PL distribution, a circular model obtained by extending the wrapped Lindley distribution by incorporating two additional shape parameters. The proposed generalisation increases flexibility in modelling concentration and skewness while preserving analytical tractability and encompassing existing circular models as special cases. Closed-form expressions for the probability density function, cumulative distribution function, and trigonometric moments are derived, allowing key distributional properties to be studied analytically. The distributional modality is characterised, and the nature of invariance is investigated for the newly proposed circular model. Parameter estimation is developed within a regularised maximum likelihood framework, and a simulation study demonstrates reliable parameter recovery and stable finite-sample performance. Applications to angular datasets from geology, marine biology, and finance illustrate the model's practical significance and show improved fit relative to existing circular alternatives.

Keywords directional, SDG goals, regularised maximum likelihood estimation, trigonometric moments, skewness and kurtosis

1 Introduction

Angular data naturally arise in many scientific and applied contexts where the variable of interest is inherently directional or periodic. Unlike linear data, where data are measured simply as positive ($x > 0$) or unbounded ($-\infty < x < \infty$), circular data wraps around (i.e., 0° and 360° represent the same direction), rendering traditional linear statistical models inadequate or misleading. When data are measured in a "non-linear" way, the accompanying probabilistic inference should correctly account for this behaviour - in this case, where data are measured as angles. Consequently, there has been a resurgence in recent years in the study of the potential probability structures underlying data distributed on the circle. Circular distributions are essential for modelling biological, geological and financial data when the variables in question exhibit such inherent periodicity, such as time of day, wind direction, animal migration orientation, or seasonal cycles. Moreover, inspired by the Sustainable Development Goals (SDGs), it is imperative that research focuses on

addressing and understanding the goals in meaningful ways. Proper use of circular statistics for circularly distributed data, especially in the environmental sciences, enables more accurate analyses and predictions, which are critical for addressing SDGs such as Goal 13: Climate Action, Goal 14: Life Below Water, and Goal 15: Life On Land. For example, understanding wind and ocean current directions using circular models supports climate modelling and marine conservation planning. This precision supports informed decision-making for sustainability and resilience in the face of environmental change.

To illustrate the practical relevance of circular models, this paper considers three datasets from distinct application areas. As one of the real data examples, we consider the dataset on travel directions of $n = 31$ blue periwinkles, as investigated by [1]. In this case, it would be relevant to marine biologists working in this field to establish the extent to which periwinkles exhibit directional preferences in their movement patterns [2]. This is meaningful as it can help determine whether periwinkles tend to move in particular directions in response to environmental cues such as tidal cycles, moisture gradients or food resources. Naturally, it is understandable that a standard "linear" PDF would not suffice to model the intricacies of data such as this, which emphasises the continued importance of wrapped models for proper statistical inference. Where circular models are formulated in radians (when $\theta \in [0, 2\pi)$), data measured in degrees should be converted to radians by multiplying the data by $\frac{\pi}{180}$ prior to model fitting.

Many authors have described and implemented the methodology of obtaining (and subsequently investigating) a distribution on the unit circle via wrapping; recent examples in the literature include [3, 4, 5, 6, 7, 8, 9, 10, 11]. In particular, [12] completed a review of recent discrete and continuous models for the circle via wrapping, and two important monographs within the circular realm are those by [13] and [14]. For a linear continuous random variable X with (continuous) infinite support with probability density function (PDF) $f(x; \alpha)$ and corresponding parameter vector α , the corresponding circular PDF of the random variable $\theta = X \bmod 2\pi$ such that $\theta \in [0, 2\pi)$ is given by

$$g(\theta; \alpha) = \sum_{m=-\infty}^{\infty} f(\theta + 2m\pi; \alpha).$$

If X has (continuous) positive support, then the circular PDF is given by

$$g(\theta; \alpha) = \sum_{m=0}^{\infty} f(\theta + 2m\pi; \alpha). \quad (1)$$

One particular example of a linear distribution that has been wrapped (and received subsequent attention, see [15]) is the Lindley distribution (see [16]), with (linear) PDF

$$f(x; \kappa) = \frac{\kappa^2}{1 + \kappa} (1 + x) \exp(-\kappa x), \quad x > 0, \kappa > 0 \quad (2)$$

(where $\alpha \equiv \kappa$) and subsequent circular PDF

$$g(\theta; \kappa) = \frac{\kappa^2}{1 + \kappa} \exp(-\kappa\theta) \left[\frac{1 + \kappa}{1 - \exp(-2\pi\kappa)} + \frac{2\pi \exp(-2\pi\kappa)}{(1 - \exp(-2\pi\kappa))^2} \right], \quad \theta \in [0, 2\pi), \kappa > 0. \quad (3)$$

The cumulative distribution function (CDF) for this distribution is given by

$$G(\theta; \kappa) = \frac{1}{1 - \exp(-2\pi\kappa)} \left(1 - \exp(-\kappa\theta) - \frac{\kappa\theta \exp(-\kappa\theta)}{\kappa + 1} \right) - \frac{2\pi\kappa}{\kappa + 1} (1 - \exp(-\kappa\theta)) \frac{\exp(-2\pi\kappa)}{(1 - \exp(-2\pi\kappa))^2}.$$

Although it is generally preferred that a distribution have fewer parameters than more, the single parameter α in this model may fall short of capturing the true intricacies of the underlying data. Here, the perceptive practitioner can foresee that κ is the single parameter that has to accurately describe the (circular) mean, variance, skewness, and kurtosis (see Appendix A.2 for these expressions) of sample data for a good fit. In the spirit of relieving this single parameter of this burden, it is of both theoretical and inferential value to investigate models which i) generalises the model in (3) where the generalised model nests this wrapped Lindley as a special case, and ii) subsequently study such a generalisation to establish the behaviour of additional parameters in a model fitting context – in order to verify such a model's validity and feasibility.

[17] introduced and studied a three-parameter Lindley distribution (referred to as the 3PL distribution); for a random variable X following this distribution, the PDF is given by

$$f(x; \kappa, \alpha, \beta) = \frac{\kappa^2}{\alpha\kappa + \beta} (\alpha + \beta x) \exp(-\kappa x), \quad x > 0, \quad \beta, \kappa > 0, \quad \alpha\kappa + \beta > 0. \quad (4)$$

with the CDF given by

$$F(x; \kappa, \alpha, \beta) = 1 - \left(1 + \frac{\kappa\beta x}{\alpha\kappa + \beta}\right) \exp(-\kappa x), \quad x > 0. \quad (5)$$

It follows immediately that, in (4), when $\alpha = \beta = 1$, the usual Lindley distribution (2) is obtained. When $\alpha = 1$, the two-parameter Lindley distribution of [18] is obtained. Considering this distribution in a circular context would be impactful, as it nests the usual Lindley distribution as a special case and provides meaningful parameter enrichment, offering additional flexibility that may better reflect the true underlying data characteristics.

In this paper, we derive and present a novel circular distribution, the wrapped 3PL (w3PL) distribution, for data distributed on the circle. The distribution and its key properties and characteristics are presented in Section 2, where the PDF, CDF, trigonometric moments, modality and property of invariance are established and investigated. In Section 3, aspects of estimation and sampling are discussed, and Section 4 presents numerical studies, including a simulation study and model fitting to three real datasets. Section 5 concludes the paper.

2 A wrapped 3PL distribution

In this section, we derive and investigate a circular companion to the linear PDF in (4) via wrapping (see (1)). The proofs for these results are outlined in Appendix A.1.

Theorem 2.1. *Suppose X follows the 3PL distribution with the PDF (4) with parameters (κ, α, β) . Then, the corresponding circular w3PL variable Θ has the following PDF:*

$$g(\theta; \kappa, \alpha, \beta) = \frac{\kappa^2}{\alpha\kappa + \beta} \frac{\exp(-\kappa\theta)}{1 - \exp(-2\pi\kappa)} \left[\alpha + \beta\theta + \frac{2\pi\beta \exp(-2\pi\kappa)}{1 - \exp(-2\pi\kappa)} \right] \quad (6)$$

where $\theta \in [0, 2\pi)$ and $\kappa, \beta > 0$ and $\alpha\kappa + \beta > 0$. Where relevant, this distribution will be denoted by w3PL. We note here that, as in the linear case, the "usual" wrapped Lindley model with PDF (3) is obtained from (6) when $\alpha = \beta = 1$ (see [15]).

Theorem 2.2. *Suppose X follows the 3PL distribution with the PDF (4) with parameters (κ, α, β) . Then, the CDF of the corresponding circular w3PL variable Θ is given by:*

$$G(\theta; \kappa, \alpha, \beta) = \left(1 - \exp(-\kappa\theta) - \frac{\kappa\beta\theta}{\alpha\kappa + \beta} \exp(-\kappa\theta)\right) \frac{1}{1 - \exp(-2\pi\kappa)} + \left(\frac{2\pi\kappa\beta}{\alpha\kappa + \beta} \{1 - \exp(-\kappa\theta)\}\right) \frac{\exp(-2\pi\kappa)}{(1 - \exp(-2\pi\kappa))^2}. \quad (7)$$

As before, the "usual" wrapped Lindley model with CDF (5) is obtained from (7) when $\alpha = \beta = 1$.

Figure 1 represents the PDF (6) and CDF (7) for different parameter configurations for κ , α , and β , respectively.

2.1 Trigonometric moments

We present a Lemma that is useful for establishing the trigonometric moments of (6).

Lemma 2.1. *Suppose a random variable X follows the 3PL distribution with the PDF (4) with parameters (κ, α, β) . Then, the characteristic function of X is given by*

$$\phi_X(t) = \frac{\kappa^2}{\alpha\kappa + \beta} \left[\frac{\alpha(\kappa - it) + \beta}{(\kappa - it)^2} \right]. \quad (8)$$

where $i = \sqrt{-1}$.

Using (8), the trigonometric moments of order p of the distribution in (6) can be established via the relation $\phi(p) = \rho_p \exp(i\mu_p) = \phi_X(t)$. This means that the characteristic function of the distribution in (6) is given by

$$\phi(p) = \frac{\kappa^2}{\alpha\kappa + \beta} \left[\frac{\alpha(\kappa - ip) + \beta}{(\kappa - ip)^2} \right].$$

Let $z = a - ib$. The polar representation of a complex number gives

$$z = r \exp(i\theta)$$

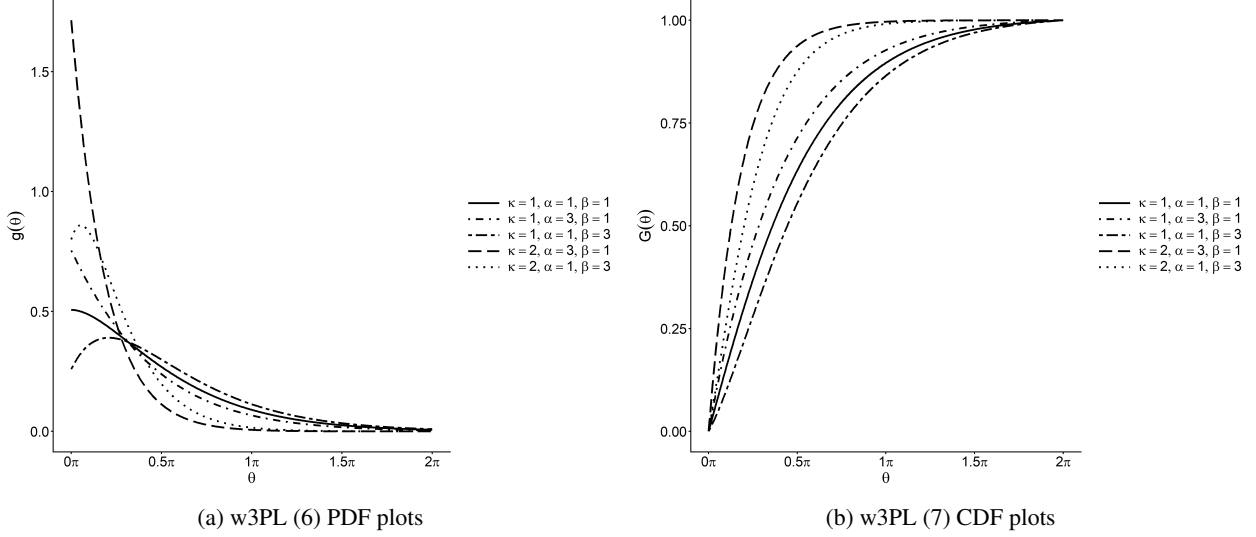


Figure 1: w3PL PDF and CDF plots for different parameter configurations

where $r = |z| = \sqrt{a^2 + b^2}$ and $\theta = \arg(z)$, as expressed in [19]. For $z = a - ib$ we have

$$\theta = \arg(a - ib) = -\arctan\left(\frac{b}{a}\right),$$

so that

$$a - ib = r \exp\left(-i \arctan\left(\frac{b}{a}\right)\right).$$

Using the exponential form of De Moivre's formula,

$$(r \exp(i\theta))^m = r^m \exp(im\theta),$$

which follows from Euler's identity $\exp(i\theta) = \cos \theta + i \sin \theta$, we obtain

$$(a - ib)^{-m} = r^{-m} \exp\left(im \arctan\left(\frac{b}{a}\right)\right). \quad (9)$$

Using (9), the characteristic function can be written as

$$\phi(p) = \frac{\kappa^2}{\alpha\kappa + \beta} \frac{((\alpha\kappa + \beta)^2 + \alpha^2 p^2)^{\frac{1}{2}}}{\kappa^2 + p^2} \exp\left(i \left(2 \arctan\left(\frac{p}{\kappa}\right) - \arctan\left(\frac{\alpha p}{\alpha\kappa + \beta}\right)\right)\right)$$

which leads to the identification of

$$\mu_p = 2 \arctan\left(\frac{p}{\kappa}\right) - \arctan\left(\frac{\alpha p}{\alpha\kappa + \beta}\right), \quad (10)$$

$$\rho_p = \frac{\kappa^2}{\alpha\kappa + \beta} \frac{((\alpha\kappa + \beta)^2 + \alpha^2 p^2)^{\frac{1}{2}}}{\kappa^2 + p^2}. \quad (11)$$

Subsequently, the noncentral trigonometric moments of the distribution in (6) can be obtained. Since the definition of trigonometric moments is given by $\phi_p = a_p + ib_p$ where $a_p = \rho_p \cos(\mu_p)$ and $b_p = \rho_p \sin(\mu_p)$, the noncentral trigonometric moments follow as

$$a_p = \frac{\kappa^2}{\alpha\kappa + \beta} \frac{((\alpha\kappa + \beta)^2 + \alpha^2 p^2)^{\frac{1}{2}}}{\kappa^2 + p^2} \cos\left(2 \arctan\left(\frac{p}{\kappa}\right) - \arctan\left(\frac{\alpha p}{\alpha\kappa + \beta}\right)\right), \quad (12)$$

$$b_p = \frac{\kappa^2}{\alpha\kappa + \beta} \frac{((\alpha\kappa + \beta)^2 + \alpha^2 p^2)^{\frac{1}{2}}}{\kappa^2 + p^2} \sin\left(2 \arctan\left(\frac{p}{\kappa}\right) - \arctan\left(\frac{\alpha p}{\alpha\kappa + \beta}\right)\right). \quad (13)$$

In particular, the *central* trigonometric moments are given by $\bar{a}_p = \rho_p \cos(\mu_p - p\mu_1)$ and $\bar{b}_p = \rho_p \sin(\mu_p - p\mu_1)$ leaving:

$$\begin{aligned}\bar{a}_p &= \frac{\kappa^2}{\alpha\kappa + \beta} \frac{((\alpha\kappa + \beta)^2 + \alpha^2 p^2)^{\frac{1}{2}}}{\kappa^2 + p^2} \\ &\quad \times \cos\left(2 \arctan\left(\frac{p}{\kappa}\right) - \arctan\left(\frac{\alpha p}{\alpha\kappa + \beta}\right) - p\left(2 \arctan\left(\frac{1}{\kappa}\right) - \arctan\left(\frac{\alpha}{\alpha\kappa + \beta}\right)\right)\right), \\ \bar{b}_p &= \frac{\kappa^2}{\alpha\kappa + \beta} \frac{((\alpha\kappa + \beta)^2 + \alpha^2 p^2)^{\frac{1}{2}}}{\kappa^2 + p^2} \\ &\quad \times \sin\left(2 \arctan\left(\frac{p}{\kappa}\right) - \arctan\left(\frac{\alpha p}{\alpha\kappa + \beta}\right) - p\left(2 \arctan\left(\frac{1}{\kappa}\right) - \arctan\left(\frac{\alpha}{\alpha\kappa + \beta}\right)\right)\right).\end{aligned}$$

As important summary measures in the circular context, the following quantities are of immediate relevance (see [13]):

- Mean direction (using (10) where $p = 1$):

$$\mu = \mu_1 = 2 \arctan\left(\frac{1}{\kappa}\right) - \arctan\left(\frac{\alpha}{\alpha\kappa + \beta}\right); \quad (14)$$

- Circular variance (using (11) where $p = 1$):

$$V_0 = 1 - \rho_1 = 1 - \rho = 1 - \frac{\kappa^2}{\alpha\kappa + \beta} \frac{((\alpha\kappa + \beta)^2 + \alpha^2)^{\frac{1}{2}}}{\kappa^2 + 1}; \quad (15)$$

- Circular deviation:

$$\sigma_0 = \sqrt{-2 \log(1 - V_0)} = \sqrt{-2 \log\left(\frac{\kappa^2}{\alpha\kappa + \beta} \frac{((\alpha\kappa + \beta)^2 + \alpha^2)^{\frac{1}{2}}}{\kappa^2 + 1}\right)};$$

- Coefficient of skewness:

$$\eta_1 = \frac{\bar{b}_2}{V_0^{\frac{3}{2}}}; \quad (16)$$

and

- Coefficient of kurtosis:

$$\eta_2 = \frac{\bar{a}_2 - (1 - V_0)^4}{V_0^2}. \quad (17)$$

Table 1 illustrates representative parameter configurations chosen to highlight distinct behavioural regimes of the w3PL distribution. Values of the (circular) mean (14), variance (15), skewness (16), and kurtosis (17) are calculated for arbitrary values of the parameters κ , α , and β . The shaded line illustrates, for example, agreement with the results of [15], showing the model proposed in that paper as a special case of the one presented in this paper. Key observations are summarised in the different groups. In Group A the concentration parameter is fixed at a small value $\kappa = 0.25$. In this regime, the distribution approaches a near-uniform baseline, reflected by large values of V_0 and shape measures η_1 and η_2 close to zero. Although variations in α and β influence the distribution, their impact is relatively mild compared to the dominant effect of a small κ . Group B exhibits the cases where the concentration parameter is fixed at $\kappa = 1$, while the shape parameters α and β are varied. Changes in these parameters lead to visible shifts in the mean direction, together with increasing departures from symmetry. As the parameter configurations become more extreme, larger magnitudes of skewness and kurtosis are observed, illustrating how the model accommodates increasingly asymmetric and heavy-tailed circular behaviour. Lastly, in Group C, the parameters α and β are held constant while κ increases across values surrounding a critical transition point. As κ increases, the mean direction moves toward zero, concentration increases (smaller V_0), and the magnitude of the higher-order shape measures grows substantially. This behaviour highlights the control that κ exerts over modal structure and distributional sharpness.

To further illustrate these relationships, the dependence of the summary measures on the concentration parameter is examined graphically. The summary measures shown in Table 1 can be observed in Figure 2, where the key summary measures with respect to the concentration parameter κ is illustrated for selected parameter configurations. Figure 2a displays the mean direction μ as a function of κ . Across all parameter configurations, the mean direction decreases

Table 1: Representative summary measures of the w3PL distribution illustrating low-concentration, shape-variation, and concentration-transition regimes.

Group	κ	α	β	μ	V_0	η_1	η_2
A	0.25	1	3	2.353	0.938	-0.014	-0.015
	0.25	1	2	2.233	0.936	-0.017	-0.016
	0.25	2	1	1.724	0.902	-0.050	-0.011
	0.25	3	1	1.609	0.883	-0.066	-0.003
B	1.00	1	1	1.107	0.441	-0.683	0.526
	1.00	1	4	1.373	0.490	-0.497	0.267
	1.00	4	1	0.896	0.360	-0.973	1.124
	1.00	1	50	1.551	0.500	-0.453	0.230
	1.00	50	1	0.795	0.300	-1.228	1.680
C	1.60	6	3	0.673	0.204	-1.815	2.657
	2.00	6	3	0.547	0.138	-2.441	4.006
	2.40	6	3	0.458	0.099	-2.982	5.236

monotonically and gradually approaches zero as κ increases, confirming the concentration parameter's dominant influence on the distribution's location. Differences between curves reflect the influence of α and β , which primarily shifts the level of the mean direction while preserving the overall trend. Figure 2b shows the circular variance V_0 . For all configurations, V_0 decreases rapidly with increasing κ , indicating increasing concentration around the modal direction. The curves show similar decay patterns, indicating that concentration is largely governed by κ , while the shape parameters introduce moderate adjustments to dispersion. The behaviour of circular skewness η_1 is illustrated in Figure 2c. Here it can be seen that as κ increases, the magnitude of skewness grows steadily, moving away from zero and indicating increasing asymmetry in the distribution. Parameter configurations associated with stronger shape effects produce more pronounced departures from symmetry, consistent with the patterns observed in Group B of Table 1. Finally, Figure 2d presents circular kurtosis η_2 . Here, we observe an increase in kurtosis as κ increases, indicating that higher concentration is associated with heavier tails and a sharper modal structure. The difference between the curves highlights how variations in α and β magnify higher-order shape characteristics, even when the overall concentration trend is controlled by κ .

While the circular mean, variance, skewness and kurtosis provide valuable insight into the overall location, dispersion and shape of the distribution, they do not directly describe the structural form of the PDF itself. A natural next step is therefore to investigate the distribution's modality and determine the conditions under which the w3PL exhibits a unique mode.

2.2 Modality of the w3PL

In this section, the modality of the w3PL distribution with PDF in (6) is formally investigated, and conditions governing the existence and location of the mode are established.

Theorem 2.3. *Suppose Θ follows the w3PL distribution with the PDF (6) with parameters (κ, α, β) . Then there exists one unique mode at the point*

$$\theta_{mode} = \frac{1}{\kappa} - \frac{\alpha}{\beta} - \frac{2\pi \exp(-2\pi\kappa)}{1 - \exp(-2\pi\kappa)}. \quad (18)$$

From (18), the critical point of the PDF in (6) is given by

$$\theta_{mode} = S(\kappa) - \frac{\alpha}{\beta}, \quad S(\kappa) := \frac{1}{\kappa} - \frac{2\pi}{\exp(2\pi\kappa) - 1}.$$

An interior mode, therefore, requires

$$0 < \theta_{mode} = S(\kappa) - \frac{\alpha}{\beta} < 2\pi,$$

which is equivalent to $0 < S(\kappa) - \alpha/\beta < 2\pi$, and particularly requires $S(\kappa) > \alpha/\beta$. To investigate the validity of this condition, we investigate the limiting behaviour of $S(\kappa)$ as $\kappa \rightarrow 0^+$ and $\kappa \rightarrow \infty$. Consider first

$$\lim_{\kappa \rightarrow 0^+} S(\kappa) = \lim_{\kappa \rightarrow 0^+} \left(\frac{1}{\kappa} - \frac{2\pi}{\exp(2\pi\kappa) - 1} \right).$$

Using the Taylor expansion

$$\exp(2\pi\kappa) = 1 + 2\pi\kappa + 2\pi^2\kappa^2 + O(\kappa^3),$$

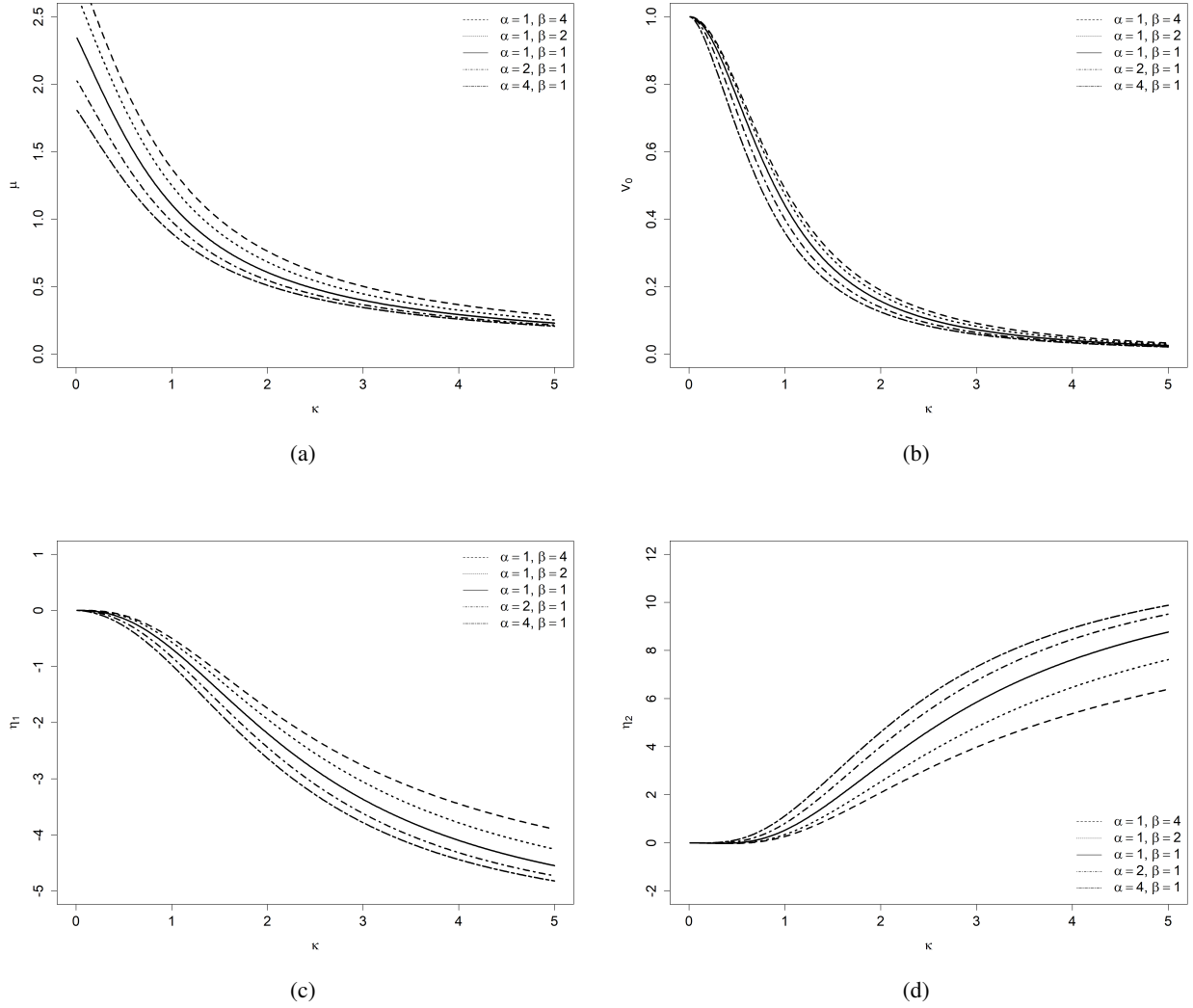


Figure 2: Summary measures of the w3PL distribution as functions of κ for selected (α, β) configurations

we obtain

$$\exp(2\pi\kappa) - 1 = 2\pi\kappa(1 + \pi\kappa + O(\kappa^2)).$$

Hence,

$$\frac{2\pi}{\exp(2\pi\kappa) - 1} = \frac{1}{\kappa} \frac{1}{1 + \pi\kappa + O(\kappa^2)}.$$

Applying the Taylor expansion of $(1+x)^{-1}$ about $x=0$,

$$(1+x)^{-1} = 1 - x + O(x^2), \quad |x| < 1,$$

yields

$$\frac{1}{1 + \pi\kappa + O(\kappa^2)} = 1 - \pi\kappa + O(\kappa^2).$$

Therefore,

$$\begin{aligned} \lim_{\kappa \rightarrow 0^+} S(\kappa) &= \lim_{\kappa \rightarrow 0^+} \left[\frac{1}{\kappa} - \frac{1}{\kappa} (1 - \pi\kappa + O(\kappa^2)) \right] \\ &= \lim_{\kappa \rightarrow 0^+} (\pi + O(\kappa)) = \pi. \end{aligned}$$

Next, as $\kappa \rightarrow \infty$, we note that $\exp(2\pi\kappa) \rightarrow \infty$, and hence

$$\lim_{\kappa \rightarrow \infty} S(\kappa) = \lim_{\kappa \rightarrow \infty} \left(\frac{1}{\kappa} - \frac{2\pi}{\exp(2\pi\kappa) - 1} \right) = 0.$$

Consequently, $S(\kappa)$ is a positive, strictly decreasing function that maps $(0, \infty)$ onto $(0, \pi)$. Let

$$r := \frac{\alpha}{\beta}, \quad 0 < r < \pi.$$

Then there exists a unique cutoff value $\kappa_r > 0$ satisfying

$$S(\kappa_r) = r.$$

For $0 < \kappa < \kappa_r$, the stationary point $\theta_{\text{mode}} = S(\kappa) - r$ lies in $(0, 2\pi)$ and corresponds to an interior mode. When $\kappa \geq \kappa_r$, the stationary point leaves the interior of the support and the maximum of the PDF occurs at the boundary $\theta = 0$.

Accordingly, the mode of the distribution on $[0, 2\pi)$ may be written in the piecewise form

$$\text{Mod}(\theta) = \begin{cases} \frac{1}{\kappa} - \frac{2\pi}{\exp(2\pi\kappa) - 1} - \frac{\alpha}{\beta}, & 0 < \kappa < \kappa_r, \\ 0, & \kappa \geq \kappa_r \text{ or } r > \pi. \end{cases}$$

The following remark clarifies the existence and uniqueness of the cutoff κ_r .

Remark 2.1. *Rewriting the condition of the interior mode yields*

$$0 < S(\kappa) - \frac{\alpha}{\beta} < 2\pi \iff \beta(S(\kappa) - 2\pi) < \alpha < \beta S(\kappa).$$

Since $\alpha > 0$, the admissible range reduces to

$$\max\{0, \beta(S(\kappa) - 2\pi)\} < \alpha < \beta S(\kappa).$$

For $\beta > 0$, the upper bound is meaningful provided $S(\kappa) > 0$. Indeed,

$$S(\kappa) > 0 \iff \frac{1}{\kappa} > \frac{2\pi}{\exp(2\pi\kappa) - 1} \iff \exp(2\pi\kappa) > 1 + 2\pi\kappa,$$

which holds for all $\kappa > 0$. Consequently, for any $r = \alpha/\beta \in (0, \pi)$ there exists a unique cutoff $\kappa_r > 0$ satisfying $S(\kappa_r) = r$, and the interior mode occurs precisely for $0 < \kappa < \kappa_r$.

In Figures 3 and 4 we observe (6) for a fixed $\alpha = 6$ and $\beta = 4$ for two different values of κ relative to the cutoff $\kappa_r = 0.6102$, which satisfies $S(\kappa_r) = 1.5$. In Figure 3 we observe the PDF for $\kappa = 0.2441 < \kappa_r$, so that the interior-mode regime is illustrated where the critical point and maximum, $\theta_{\text{mode}} = 0.8681$, lies within $[0, 2\pi)$. In contrast, Figure 4 shows the PDF for $\kappa = 0.7322 > \kappa_r$, so that the boundary-mode regime is illustrated where the critical point leaves the interior of the support and the PDF is maximised at $\theta_{\text{mode}} = 0$.

While the preceding analysis establishes the modality of the w3PL distribution, an additional property of interest in circular models is their behaviour under transformations of the reference system. It is particularly desirable that a circular distribution maintains a coherent probabilistic structure under rotations on the circle.

2.3 The property of invariance

In this section, the invariance property of the w3PL distribution is examined using the framework developed by [20].

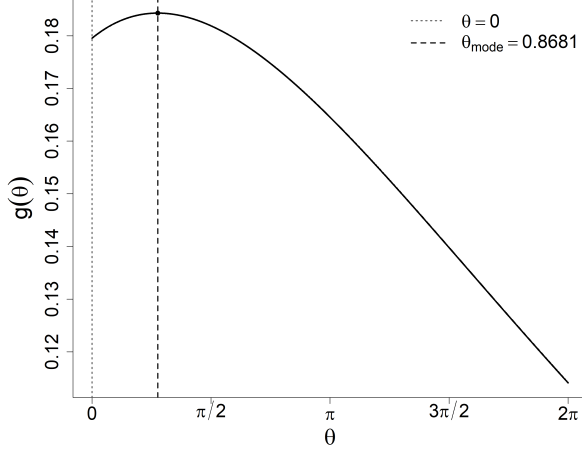
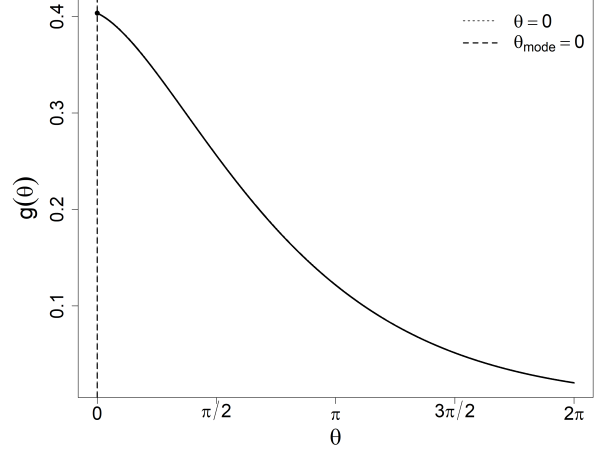
Theorem 2.4. *Let $\mathbb{T} = [a, b)$ with $b - a = 2\pi$, and let $\Theta \in \mathbb{T}$ be a circular random variable with PDF $g_{\Theta}(\cdot; \psi)$, where $\psi \in \Psi$ is a parameter vector. Define a transformed variable*

$$\Theta^* = \delta(\Theta + \epsilon), \quad \delta \in \{-1, 1\}, \quad \epsilon \in \mathbb{T},$$

and let $g_{\Theta^}(\cdot; \psi^*)$ be the PDF of Θ^* , with $\psi^* \in \Psi^*$. Then g_{Θ} is invariant under changes in orientation (ICO) and invariant under changes in initial direction (ICID) if and only if*

$$g_{\Theta^*}(\theta^*; \psi^*) = g_{\Theta}(\theta^*; \psi) \quad \text{for almost every } \theta^* \in \mathbb{T},$$

with $\Psi^ \equiv \Psi$, in the sense that the characteristic functions of Θ and Θ^* must belong to the same functional family.*


Figure 3: Interior-mode regime when $0 < \kappa < \kappa_r$

Figure 4: Boundary-mode regime when $\kappa \geq \kappa_r$

We will now show that the w3PL distribution is not invariant, but can be transformed to meet the requirements. The characteristic function of θ^* for the w3PL distribution is provided by

$$\begin{aligned}
\phi_{\theta^*}(p) &= E(\exp(ip\theta^*)) \\
&= E(\exp(ip[\delta(\theta + \epsilon)])) \\
&= E(\exp(i\delta p\theta + i\delta p\epsilon)) \\
&= \exp(i\delta p\epsilon)E(\exp(i\delta p\theta)) \\
&= \exp(i\delta p\epsilon)\phi_{\theta}(\delta p)
\end{aligned}$$

It was previously stated that $\phi_{\theta}(p) = a_p + ib_p$ so that $\phi_{\theta}(\delta p) = a_{\delta p} + ib_{\delta p}$. Note that a_p and b_p were defined in (12) and (13), respectively, and that

$$\begin{aligned}
a_{\delta p} &= \frac{\kappa^2}{\alpha\kappa + \beta} \frac{((\alpha\kappa + \beta)^2 + \alpha^2 p^2)^{\frac{1}{2}}}{\kappa^2 + p^2} \cos\left(2 \arctan\left(\frac{\delta p}{\kappa}\right) - \arctan\left(\frac{\alpha\delta p}{\alpha\kappa + \beta}\right)\right) \\
b_{\delta p} &= \frac{\kappa^2}{\alpha\kappa + \beta} \frac{((\alpha\kappa + \beta)^2 + \alpha^2 p^2)^{\frac{1}{2}}}{\kappa^2 + p^2} \sin\left(2 \arctan\left(\frac{\delta p}{\kappa}\right) - \arctan\left(\frac{\alpha\delta p}{\alpha\kappa + \beta}\right)\right).
\end{aligned}$$

Using Euler's formula (see [19]) we obtain

$$\exp(i\delta p\epsilon) = \cos(\delta p\epsilon) + i \sin(\delta p\epsilon),$$

so that

$$\begin{aligned}
\phi_{\theta^*}(p) &= (\cos(\delta p\epsilon) + i \sin(\delta p\epsilon))(a_{\delta p} + ib_{\delta p}) \\
&= a_{\delta p} \cos(\delta p\epsilon) - b_{\delta p} \sin(\delta p\epsilon) + i(a_{\delta p} \sin(\delta p\epsilon) + b_{\delta p} \cos(\delta p\epsilon))
\end{aligned}$$

which will be equal to $\phi_{\theta}(p)$ if and only if $\delta = 1$ and $\epsilon = 0$. Within these specific requirements, we conclude that $g_{\Theta}(\cdot; \psi)$ is not ICO and ICID. The PDF $g_{\Theta^*}(\cdot; \psi^*)$, with $\Theta^* = \delta(\Theta + \epsilon)$, $\delta \in \{-1, 1\}$, $\epsilon \in \mathbb{T}$, and $\psi^* = (\psi, \delta, \epsilon) \in \Psi^*$ is, however, ICO and ICID, according to [20]. We can rewrite $\Theta^* = \delta(\Theta + \epsilon)$ in terms of Θ so that $\Theta = \delta^{-1}\Theta^* - \epsilon$. Therefore, with this transformation,

$$\begin{aligned}
g_{\Theta^*}(\theta^*; \delta, \epsilon, \kappa, \alpha, \beta) &= \left| \frac{d\theta}{d\theta^*} \right| g_{\Theta}(\delta^{-1}\theta^* - \epsilon; \kappa, \alpha, \beta) \\
&= \left| \frac{d(\delta^{-1}\theta^* - \epsilon)}{d\theta^*} \right| g_{\Theta}(\delta^{-1}\theta^* - \epsilon; \kappa, \alpha, \beta) \\
&= |\delta^{-1}| g_{\Theta}(\delta^{-1}\theta^* - \epsilon; \kappa, \alpha, \beta) \\
&= 1 \cdot g_{\Theta}(\delta\theta^* - \epsilon; \kappa, \alpha, \beta) \quad \text{since } \delta \in \{-1, 1\} \\
&= \frac{\kappa^2 \exp(-\kappa(\delta\theta^* - \epsilon))}{\alpha\kappa + \beta} \left[\alpha + \beta(\delta\theta^* - \epsilon) + \frac{2\pi\beta \exp(-2\kappa\pi)}{1 - \exp(-2\kappa\pi)} \right],
\end{aligned}$$

so that the invariant family can be expressed as

$$\{g_{\Theta}(\delta\theta - \epsilon; \kappa, \alpha, \beta) : \delta \in \{-1, 1\}, \epsilon \in [0, 2\pi)\}.$$

Having established key structural properties of the w3PL distribution, attention now turns to statistical inference, where procedures for parameter estimation and sampling from the model are developed.

3 Estimation and sampling

In this section, we outline the estimation framework for the w3PL distribution and describe the sampling and simulation design used to assess parameter recovery. We first present the maximum likelihood estimator and its regularised extension in Section 3.1, and thereafter detail the sampling scheme employed to generate data for evaluating finite-sample performance in Section 3.2.

3.1 Estimation using maximum likelihood

Suppose that $(\theta_1, \dots, \theta_n)$ is a random sample from the w3PL distribution with PDF in (6). The likelihood function is then given by

$$\begin{aligned}
&L(\kappa, \alpha, \beta | \theta_1, \dots, \theta_n) \\
&= \prod_{i=1}^n g(\theta_i; \kappa, \alpha, \beta) \\
&= \prod_{i=1}^n \frac{\kappa^2}{\alpha\kappa + \beta} \exp(-\kappa\theta_i) \left[\frac{\alpha + \beta\theta_i}{1 - \exp(-2\kappa\pi)} + \frac{2\beta\pi \exp(-2\kappa\pi)}{(1 - \exp(-2\kappa\pi))^2} \right] \\
&= \frac{\kappa^{2n}}{(\alpha\kappa + \beta)^n} \exp\left(-\kappa \sum_{i=1}^n \theta_i\right) \prod_{i=1}^n \left[\frac{\alpha + \beta\theta_i}{1 - \exp(-2\kappa\pi)} + \frac{2\beta\pi \exp(-2\kappa\pi)}{(1 - \exp(-2\kappa\pi))^2} \right]
\end{aligned}$$

from where the log-likelihood (LL) follows as

$$\begin{aligned}
&LL(\kappa, \alpha, \beta | \theta_1, \dots, \theta_n) \\
&= 2n \log(\kappa) - n \log(\alpha\kappa + \beta) - \kappa \sum_{i=1}^n \theta_i + \sum_{i=1}^n \log \left[\frac{\alpha + \beta\theta_i}{1 - \exp(-2\kappa\pi)} + \frac{2\beta\pi \exp(-2\kappa\pi)}{(1 - \exp(-2\kappa\pi))^2} \right]
\end{aligned}$$

where \log denotes the natural logarithm. Closed-form solutions to the score equations are not tractable; therefore, maximum likelihood estimates (MLEs) are obtained via numerical optimisation. The parameter space is restricted to $\kappa > 0$, $\alpha > 0$, and $\beta > 0$. In practice, optimisation is performed in log-parameters to enforce positivity constraints. Computation is carried out in R using the `optim` function with the L-BFGS-B algorithm.

To ensure inference is reliable and efficient, we employ a regularised maximum likelihood approach to estimate the parameters of the w3PL distribution. Regularisation plays an important role in likelihood-based inference for directional and circular models, particularly in settings where the likelihood may be irregular, flat or poorly behaved. As noted by [21], regularisation, or a penalised likelihood approach, is commonly used in likelihood-based estimation to *circumvent* unboundedness in mixture likelihoods and to possibly reduce overfitting. It can improve small-sample generalisation and stabilise numerical optimisation, thereby yielding better-behaved estimators.

In mixtures of von Mises-Fisher distributions, [22] shows that their likelihood function is unbounded from above so that a global MLE fails to exist. To overcome this, a penalty term is introduced so that the resulting penalised likelihood function is bounded and the existence of the penalised MLE is guaranteed. Similarly, in testing homogeneity for mixtures of von-Mises distributions, [23] adds a penalty term to the LL function to obtain a tractable limiting distribution. In multivariate circular modelling, [24] highlights that penalising model complexity helps avoid overfitting when the number of samples is relatively small compared to the number of model parameters, and proposes Frobenius-norm regularisation for the multivariate von Mises distribution. These results illustrate that penalised likelihood methods are well established in directional statistics for controlling model complexity and ensuring stable estimation. In line with this literature, we now introduce an L2-regularised maximum likelihood estimator (L2-RMLE) for the w3PL distribution and investigate its behaviour through simulation and parameter recovery.

We propose the L2-RMLE, which optimises the LL in a numerically stable manner while adding a quadratic shrinkage term to mitigate instability in finite samples for inferring from a w3PL distribution. The regularised objective augments the negative LL with a L2-RMLE in log-space, shrinking parameters toward chosen targets (α_0, β_0) , defined as follows:

$$\Delta = -LL(\kappa, \alpha, \beta | \theta_1, \dots, \theta_n) + \lambda_\alpha (\log \alpha - \log \alpha_0)^2 + \lambda_\beta (\log \beta - \log \beta_0)^2.$$

Since the penalty is quadratic in the log-parameters, the estimator remains an L2-RMLE, but applied in the transformed parameter space. Consequently, multiplicative deviations, rather than additive deviations, are shrunk, which is natural for positive scale-like parameters. The penalty weights stabilise the optimisation and constrain the estimator away from regions where the likelihood is nearly flat or the data provide weak identification of (α, β) combinations. By pulling estimates toward sensible targets, the penalty reduces variance and often lowers the MSE, even though it introduces bias. This approach trades a small, controlled bias for substantial variance reduction. In this approach, the penalty weights are scaled by the sample size so that shrinkage weakens as n increases, ensuring that the estimator asymptotically approaches the classic MLE as $n \rightarrow \infty$, under identifiability. By adopting a vanishing regularisation schedule $\lambda_i = \frac{c}{n}$ for $i = \alpha, \beta$, we obtain stabilisation in small samples while ensuring that the penalty influence diminishes as n increases. The constant c is selected to achieve stable convergence with minimal shrinkage. It is important to note that L2-RMLE is sensitive to the choice of penalty weights. If λ_i is too large or does not decay with an increase in the sample size n , the estimator can be dominated by the penalty and track the ‘target’ rather than the data.

In executing the L2-RMLE, a multistart approach is employed, providing a practical globalisation strategy that reduces dependence on initialisation and helps avoid convergence to flat ridges of the likelihood surface, an observed feature of this model. The multistart approach is based on K random initial points drawn from broad parameter ranges and a bounded quasi-Newton optimiser (L-BFGS-B) run from each initial point. The solution with the lowest objective value is retained.

3.2 Sampling and simulation design

To evaluate estimator performance under controlled conditions, samples are generated from the w3PL distribution using a numerical implementation of the inverse transform method. Since repeated root-solving of the theoretical CDF in (7) proved computationally unstable, inversion is performed numerically by constructing a monotone grid-based approximation to the inverse CDF. For fixed (κ, α, β) the analytic CDF $G(\theta)$ is evaluated on a dense grid $\theta_1, \dots, \theta_m$ spanning $[0, 2\pi)$. Since finite-precision evaluation can introduce non-monotonicities or values slightly outside $[0, 1]$, the grid CDF values are clamped to $[0, 1]$, and monotonicity is then enforced by applying a cumulative maximum operator, ensuring a nondecreasing CDF. The grid is then thinned by removing near-duplicate CDF levels so that inversion is stable. The resulting strictly increasing pairs $\{(F_i, \theta_i)\}$ define a numerical approximation to the inverse CDF via linear interpolation. Sampling reduces to drawing $U \sim \text{Unif}(0, 1)$ and returning $\theta = \hat{F}^{-1}(U)$.

To examine parameter recovery, samples of sizes $n = 50, 100, 250$ and 500 are generated under fixed parameter configurations. For each of these configurations, we obtain the corresponding L2-regularised maximum likelihood estimates of κ, α , and β . The procedure is repeated $N = 200$ times for each sample size. Let λ^* denote the true parameter value. Performance is evaluated using empirical bias and mean squared error (MSE), defined as

$$\begin{aligned} \text{bias}(\hat{\lambda}) &= \frac{1}{N} \sum_{i=1}^N (\hat{\lambda} - \lambda^*) \\ \text{MSE}(\hat{\lambda}) &= \frac{1}{N} \sum_{i=1}^N (\hat{\lambda} - \lambda^*)^2 \end{aligned}$$

These metrics quantify systematic deviation from the truth and overall estimation accuracy, respectively.

4 Numerical examples

In this section, we evaluate the finite-sample performance of the w3PL distribution through a simulation experiment, followed by applications to real circular datasets. The simulation study in Section 4.1 focuses on parameter recovery under both interior- and boundary-mode regimes to assess estimation accuracy and stability across distinct regions of the parameter space. In addition, we examine how estimation behaviour changes with increasing sample size, providing insight into convergence trends. Three real data applications are presented in Section 4.2 to illustrate the model’s practical applicability.

4.1 Simulation studies

We evaluate the performance of the w3PL distribution in a simulation setting. Tables 2 to 5 investigate different parameter configurations, using grid-inversion with L2-RMLE, to illustrate both interior- and boundary-mode regimes for the model. In all cases, initial values were generated within a multistart framework. For the L2-RMLE, the shrinkage targets in log-space were set to the logarithm of the initial values, i.e., $\log(\alpha_0)$ and $\log(\beta_0)$. This choice centres the penalty locally around plausible parameter magnitudes while avoiding shrinkage toward arbitrary fixed constants. Based on preliminary sensitivity analyses, a constant $c = 0.5$ was selected across all configurations to achieve stable convergence with minimal shrinkage. Each table is based on $N = 200$ Monte Carlo replicates, with sample sizes ranging from $n = 50$ to 500.

We consider four representative parameter configurations that deliberately span both interior- and boundary-mode regimes. By including both regimes, we ensure that the simulation study accurately reflects the model’s geometric structure. The parameter configurations considered are:

- $(\kappa, \alpha, \beta) = (1, 2, 5)$, an interior-mode regime where $\kappa < \kappa_r = 2.5$ (Table 2)
- $(\kappa, \alpha, \beta) = (4, 1, 8)$, an interior-mode regime where $\kappa < \kappa_r = 8$ (Table 3)
- $(\kappa, \alpha, \beta) = (2, 4, 1)$, a boundary-mode regime where $r > \pi$ (Table 4)
- $(\kappa, \alpha, \beta) = (8, 1, 6)$, a boundary-mode regime where $\kappa > \kappa_r = 6$ (Table 5)

Table 2: Parameter recovery for the interior-mode configuration, $(\kappa, \alpha, \beta) = (1, 2, 5)$.

n	Parameter	Estimate	SD	Bias	MSE
50	κ	0.942	0.206	-0.058	0.045
	α	2.572	1.364	0.572	2.151
	β	6.721	7.714	1.721	11.279
100	κ	0.926	0.162	-0.074	0.031
	α	2.566	1.594	0.566	2.811
	β	5.417	2.627	0.417	6.938
250	κ	0.885	0.090	-0.115	0.021
	α	2.675	0.765	0.675	1.030
	β	4.238	1.187	-0.762	1.962
500	κ	0.900	0.063	-0.100	0.014
	α	2.489	0.518	0.489	0.502
	β	4.391	0.859	-0.609	1.095

Across the four configurations, the simulation results reveal a distinction between interior- and boundary-mode regimes. In the interior-mode settings, captured in Tables 2 and 3, parameter recovery is stable and improves consistently with increasing sample size. For both configurations, bias and variability decrease as n increases, with the concentration parameter κ generally well estimated even in moderate samples. The parameters α and β exhibit more dispersion in small samples, with variance contracting steadily, leading to reductions in MSE and convergence toward the true values. The boundary-mode configurations, captured in Tables 4 and 5, display greater instability, especially for α and β . While κ remains reasonably well recovered across sample sizes, estimation of especially α shows elevated variability and slower MSE reduction, reflecting the flatter, ridge-like geometry of the likelihood when the mode lies on or near the boundary of the support. Despite these observations, increasing the sample size improves stability and reduces error. Overall, the results indicate that the w3PL distribution is reliably estimable in interior-mode regimes and practically workable in boundary-mode settings, despite greater finite-sample variability.

Table 3: Parameter recovery for the interior-mode configuration, $(\kappa, \alpha, \beta) = (4, 1, 8)$.

n	Parameter	Estimate	SD	Bias	MSE
50	κ	4.143	0.651	0.143	0.435
	α	1.087	0.454	0.087	0.210
	β	9.532	5.670	1.532	13.847
100	κ	4.115	0.456	0.115	0.217
	α	0.987	0.392	-0.013	0.151
	β	9.870	3.781	1.871	7.511
250	κ	3.971	0.258	-0.029	0.066
	α	1.074	0.219	0.074	0.052
	β	8.153	1.704	0.153	2.868
500	κ	3.997	0.183	-0.003	0.033
	α	1.034	0.156	0.034	0.025
	β	8.308	1.252	0.308	1.631

Table 4: Parameter recovery for the boundary-mode configuration, $(\kappa, \alpha, \beta) = (2, 4, 1)$.

n	Parameter	Estimate	SD	Bias	MSE
50	κ	2.302	0.507	0.302	0.343
	α	2.133	1.209	-1.867	4.916
	β	1.589	1.207	0.589	1.775
100	κ	2.272	0.440	0.272	0.264
	α	2.836	1.714	-1.164	4.232
	β	1.257	0.934	0.257	0.921
250	κ	2.053	0.318	0.052	0.102
	α	3.950	2.249	-0.050	4.960
	β	0.845	0.585	-0.155	0.360
500	κ	2.064	0.232	0.064	0.057
	α	4.059	2.816	0.058	2.775
	β	0.831	0.495	-0.169	0.269

Table 5: Parameter recovery for the boundary-mode configuration, $(\kappa, \alpha, \beta) = (8, 1, 6)$.

n	Parameter	Estimate	SD	Bias	MSE
50	κ	8.092	1.514	0.092	2.254
	α	1.077	0.679	0.077	0.458
	β	7.195	5.222	1.195	18.150
100	κ	8.237	1.418	0.237	2.028
	α	1.213	0.905	0.213	0.848
	β	6.426	3.506	0.426	12.226
250	κ	7.802	0.943	-0.198	0.911
	α	1.157	0.609	0.157	0.388
	β	5.430	1.925	-0.570	3.954
500	κ	7.990	0.634	-0.010	0.394
	α	1.076	0.811	0.076	0.651
	β	5.629	1.313	-0.371	1.827

4.2 Real data

In this section, we investigate the behaviour of the w3PL distribution by applying it to three real-world datasets, namely the cross-bed measurements (Section 4.2.1), travel directions of blue periwinkles (Section 4.2.2), and credit-card transaction timestamps (Section 4.2.3). Model performance is ranked via the Akaike information criterion (AIC; [25]),

$$\text{AIC} = 2k - 2LL(\hat{\kappa}, \hat{\alpha}, \hat{\beta}),$$

the corrected Akaike information criteria (AICc; [26]) for small samples,

$$\text{AICc} = \text{AIC} + \frac{2k(k+1)}{n-k-1},$$

and the Bayesian information criterion (BIC; [27]),

$$\text{BIC} = \log(n)k - 2LL(\hat{\kappa}, \hat{\alpha}, \hat{\beta}),$$

where k is the number of parameters and n is the number of observations, $\hat{\kappa}$, $\hat{\alpha}$, and $\hat{\beta}$ are the ML estimates of κ , α , and β , respectively, and where $LL(\hat{\kappa}, \hat{\alpha}, \hat{\beta})$ is the maximized LL value for the model. In this formulation of both the AIC and BIC cases, the model with the smallest value is considered the preferred model. Where relevant, this is indicated in the results with the smallest value indicated in **bold**.

To illustrate the viability of the model in (6) as a meaningful alternative within the circular framework, we benchmark it to similar models as those considered in [15] and [5]. Specifically, we compare it via the AIC and BIC with the wrapped Lindley (wL) model (3), the wrapped XLindley (wXL) model of [5] with PDF

$$g(\theta; \kappa) = \frac{\kappa^2 \exp(-\theta\kappa)}{(\kappa + 1)^2 (1 - \exp(-2\pi\kappa))^2} [(1 - \exp(-2\pi\kappa))(\kappa + \theta + 2) + 2\pi \exp(-2\pi\kappa)], \theta \in [0, 2\pi), \kappa > 0, \quad (19)$$

and the wrapped exponential (wExp) model of [28] with PDF

$$g(\theta; \kappa) = \frac{\kappa \exp(-\kappa\theta)}{1 - \exp(-2\pi\kappa)}, \quad \theta \in [0, 2\pi), \kappa > 0. \quad (20)$$

The notation of the parameter κ is kept uniform throughout these models for notational simplicity; however, we note that, in a model such as (20), the role of κ differs by design from that in other considered models, where it serves as the "original" Lindley parameter. The datasets used in this paper were initially introduced and made available by [13] and are easily accessible in R via the `circular` package.

4.2.1 Cross-bed measurements

Cross-stratification is a primary sedimentary structure used to infer palaeoflow directions. The geometry of trough or planar cross-beds is linked to the migration of dunes under a prevailing flow, so that collections of measured orientations yield a directional sample that can be analysed to reconstruct flow regimes and sediment transport patterns, as described by [29]. The dataset under consideration contains $n = 104$ observations of cross-bed orientations from the Himalayan molasse in Pakistan, specifically the Chaudan Zam large bedforms, and is available as `cross.beds2` in the R package, `NPcirc`, reported in [13].

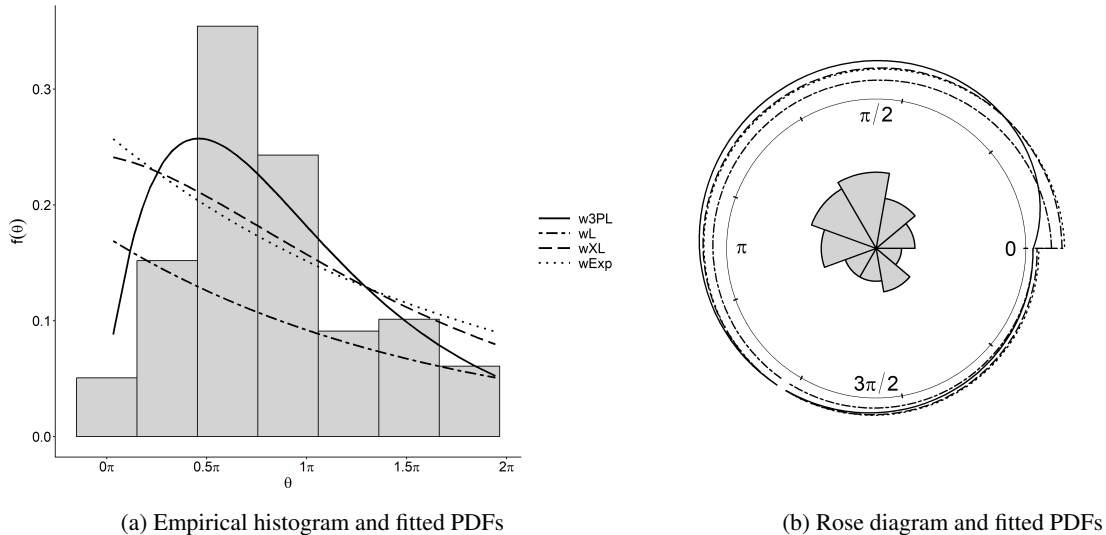


Figure 5: Model fits to the cross-bed measurement data

We fit the proposed w3PL distribution alongside the considered contenders, with results summarised in Table 6. Based on both AIC and BIC, the w3PL provides the strongest empirical fit for these data. The improvement in information criteria is substantial; relative to the next-best contender (wXL), the AIC difference exceeds 10 units, providing strong evidence in favour of the additional flexibility introduced by the w3PL's two shape parameters. The fitted model

Table 6: Results of MLE to the cross-bed data according to the AIC and BIC.

Parameter/Measure	w3PL (6)	wL (3)	wXL (19)	wExp (20)
κ	0.637	0.200	0.361	0.174
α	0.833	-	-	-
β	119.992	-	-	-
LL	-177.094	-236.521	-184.259	-186.125
AIC	360.189	475.041	370.517	374.250
BIC	368.122	477.686	373.162	376.894

comparisons are shown in Figure 5. The empirical histogram and rose diagram suggest a unimodal pattern with moderate dispersion and mild asymmetry. amongst fitted models, the w3PL PDF most closely follows the observed peak location and overall pattern, while the competing models either under-represent the concentration around the dominant direction or produce less accurate tail behaviour. This is consistent with the superior AIC and BIC values reported in Table 6.

4.2.2 Travel directions of blue periwinkles

[30] describes periwinkles as abundant intertidal grazers that influence community structure by feeding on algae and other organisms on rocky shores and marsh grasses. Their grazing can alter algal abundance and distribution, affecting habitat structure and other species in the food web. Movement studies have revealed that distance and direction are often correlated with habitat structure, sensory cues, and ecological pressures, making this type of data biologically significant, as explained by [2]. The dataset under consideration contains $n = 31$ blue periwinkles, for which the direction of displacement was recorded after individuals were transferred downshore from the heights at which they normally live, as described in [1]. The data are available in the `periwinkles` dataset of the R package, `NPCirc`.

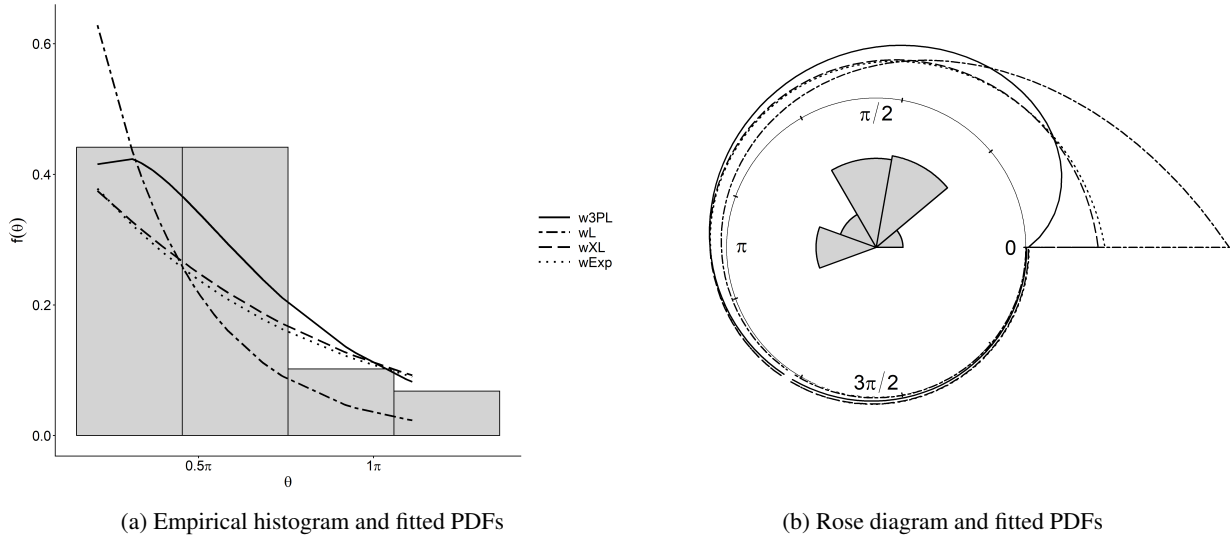


Figure 6: Model fits to the travel directions of blue periwinkles

Table 7: Results of MLE to the periwinkle data according to the AIC and BIC.

Parameter/Measure	w3PL (6)	wL (3)	wXL (19)	wExp (20)
κ	1.155	1.165	0.708	0.508
α	0.944	-	-	-
β	105.974	-	-	-
LL	-37.988	-51.837	-45.409	-46.462
AICc	82.865	105.811	92.955	95.062
BIC	86.278	107.108	94.251	96.358

We fit the proposed w3PL, alongside the competing wrapped distributions, with results summarised in Table 7. Based on both the AICc and BIC, the w3PL provides the strongest empirical fit amongst the considered models. The improvement

in AICc relative to the next-best competitor is substantial, indicating strong support for the additional flexibility provided by the two-parameter shape structure of the w3PL. Given the relatively small sample size, the use of AICc is appropriate, and the agreement between AICc and BIC strengthens the robustness of the selection. The fitted parameters indicate a moderate concentration, along with asymmetry in the data. Figure 6 highlights the superiority of the w3PL fit, where the empirical histogram and corresponding rose diagram suggest a unimodal but skewed pattern. The w3PL most closely tracks the observed peak location and asymmetric decay from the mode, while the competing models either over-concentrate around the peak or fail to capture the tail behaviour in the sample.

4.2.3 Credit-card transaction timestamp data

Transaction timestamp data reflect regular patterns in consumer behaviour and system usage, with time-of-day having shown to be an informative predictor in credit card fraud detection and transaction modelling, as highlighted by [31] and [32]. Because the 24-hour clock is inherently periodic, timestamps reduced to hour-of-day form a circular variable, where 23:00 and 00:00 are adjacent. The dataset considered here consists of $n = 349$ transactions with timestamps occurring between 1 January and 29 July 2020, obtained via the PyCircular package in Python. Transactions were filtered by transaction type (types 1 and 2) and converted to circular observations representing time of day; i.e., transaction timestamps were parsed to a date-time format and binned to the hour of day $h \in \{0, \dots, 23\}$. Hourly frequencies were computed, and each hour was encoded as an equally spaced circular angle via $\theta(h) = 2\pi h/24$, equivalent to $15h$ degrees. An observation-level circular sample was formed by repeating each hour-angle according to its hourly count. The resulting sample represents transaction intensity over the 24-hour cycle and may exhibit asymmetric concentration due to peak activity periods.

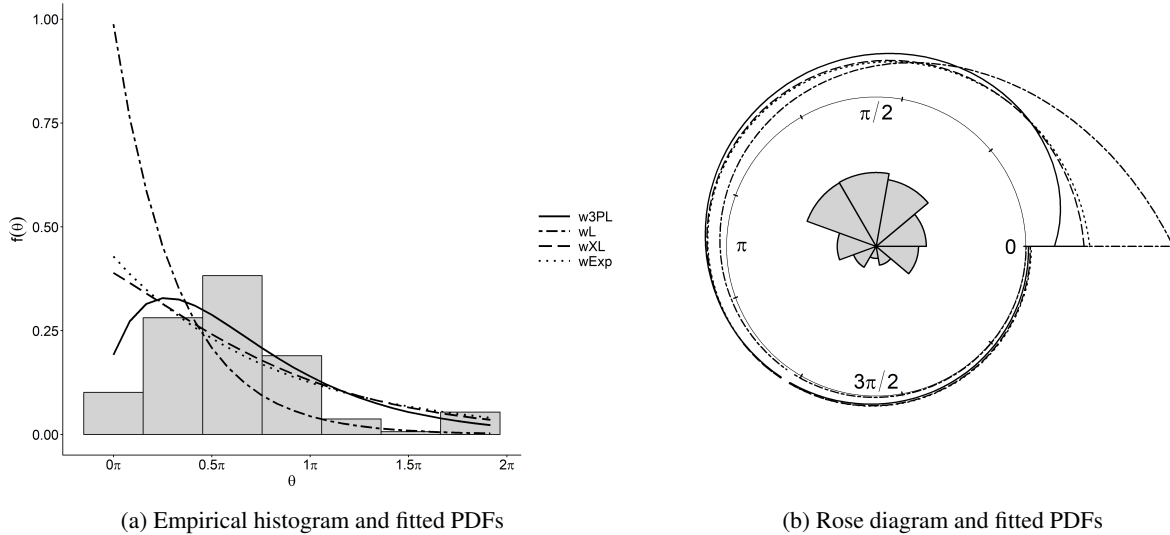


Figure 7: Model fits to the credit-card transaction timestamp data

Table 8: Results of MLE to the credit-card transaction timestamp data according to the AIC and BIC.

Parameter/Measure	w3PL (6)	wL (3)	wXL (19)	wExp (20)
κ	0.842	0.990	0.592	0.392
α	5.536	-	-	-
β	18.063	-	-	-
LL	-487.804	-608.870	-498.228	-503.193
AIC	981.609	1219.741	998.457	1008.385
BIC	992.828	1223.481	1002.197	1012.125

We fit our proposed model, the w3PL, alongside the considered contenders, and summarise the results in Table 8. Based on both AIC and BIC, the w3PL provides the strongest empirical fit. Notably, the AIC difference between the w3PL and the next-best competitor exceeds 15 units, providing strong evidence in favour of the additional flexibility introduced by the model's two-parameter shape structure. The BIC results lead to the same conclusion, reinforcing the robustness of the selection. The estimated w3PL parameters indicate a moderate concentration and a pronounced asymmetric component, governed by α and β , within the interior-mode regime. The findings in Table 8 are reflected in Figure 7,

where the empirical histogram and corresponding circular rose diagram indicate a unimodal distribution of transaction times with moderate concentration and noticeable skewness. Amongst the fitted models, the w3PL PDF aligns most closely with the observed peak location and overall pattern, capturing the asymmetric shape more effectively than the competing wrapped distributions.

5 Conclusion

In this paper, we derived, presented, and studied a previously unconsidered flexible wrapped distribution, namely the w3PL distribution. An immediate generalisation of the wrapped Lindley model of [15], our proposition uses the 3PL distribution of [33] as the linear basis in a wrapping context and nests the wrapped Lindley model as a special case. In particular, the PDF, CDF, and trigonometric moments were derived in closed form, yielding expressions for calculating key circular characteristics, including the circular mean, variance, skewness, and kurtosis. The w3PL distribution (6) achieves increased flexibility through the additional two shape parameters α and β , in addition to the parameter κ , which the model inherited from the classical Lindley and wrapped Lindley distributions. The inclusion of the parameters α and β allows additional parameters to govern the higher-order moments of the distribution, thereby providing greater control over skewness and kurtosis while retaining the structural simplicity of the wrapped Lindley framework. At the same time, the model remains tractable and computationally feasible. Simulation from the w3PL distribution is computationally feasible, and likelihood-based parameter estimation can be implemented in a stable and practical manner within a regularised framework. Considering these advantages, it is worth noting that the proposed distribution closely aligns with the desirability guidelines for flexible distributions outlined by [34].

The theoretical properties were juxtaposed with those of the wrapped Lindley model, showcasing the advantage of the additional parameters α and β . In particular:

- α and β give access to a broader range of skewness and kurtosis for the practitioner, enhancing descriptive flexibility;
- the model is reliable in parameter recovery across different sample sizes and regime configurations, including both interior- and boundary-mode settings; and
- The model is convenient to implement in practice for fitting real circular datasets.

In the simulation study, we observed that estimation accuracy improves with increasing sample size, with empirical bias and MSE generally decreasing as n grows. The L2-RMLE approach stabilised estimation in regions where the likelihood surface exhibits flat ridges, while maintaining asymptotic consistency. Overall, the simulation results confirm that the w3PL distribution can numerically recover the true parameter values with satisfactory accuracy across a range of configurations.

Finally, across three real data fitting scenarios, the w3PL distribution proved a viable contender in the circular modelling space. Across the applications, the w3PL showed superior performance, as measured by common model performance metrics: AIC, AICc, and BIC. The improvements were particularly evident in datasets exhibiting asymmetric concentration, where the additional shape flexibility of the w3PL translated into tangible gains in descriptive accuracy.

The theoretical tractability, simulation performance, and empirical competitiveness of the w3PL distribution suggest that it provides a useful and flexible addition to practitioners' toolkits of wrapped distributions for modelling asymmetric circular data.

Acknowledgments

Ferreira has been partially supported by the National Research Foundation (NRF) of South Africa (SA), grants RA201125576565 (nr 145681) and CSRP250220299317, as well as the DSI-NRF Centre of Excellence in Mathematical and Statistical Sciences (CoE-MaSS), South Africa. Van Wyk-de Ridder acknowledges the support of the Faculty of Science at the University of Cape Town, as well as the Centre for Statistics in Ecology, the Environment and Conservation, based at the University of Cape Town. The opinions expressed and conclusions arrived at are those of the authors and are not necessarily to be attributed to the NRF.

Data availability statement

All datasets considered in this paper are freely available, particularly available in the R package `circular` or `NPCirc` (which can be found in hardcopy in [13]) or in Python. The names of the datasets in this package are reported in the Real Data Application section.

Disclosure statement

The authors declared no potential conflicts of interest with respect to the research, authorship, and/or publication of this article.

Author contributions

All authors contributed to the study conception and design. Material preparation and data analysis were performed by Ferreira, van Wyk-de Ridder and van Niekerk. The first draft of the manuscript was written by Ferreira, and all authors commented and contributed to earlier versions. All authors read and approved the final manuscript.

Appendix A Proofs and other expressions

A.1 Characteristics of the w3PL distribution (6)

Proof of Theorem 2.1. By using (1) and (4), we see that

$$\begin{aligned} g(\theta; \kappa, \alpha, \beta) &= \sum_{m=0}^{\infty} f(\theta + 2m\pi; \kappa, \alpha, \beta) \\ &= \sum_{m=0}^{\infty} \frac{\kappa^2}{\alpha\kappa + \beta} (\alpha + \beta(\theta + 2m\pi)) \exp(-\kappa(\theta + 2m\pi)) \\ &= \frac{\kappa^2}{\alpha\kappa + \beta} \exp(-\kappa\theta) \left[\frac{(\alpha + \beta\theta)}{1 - \exp(-2\pi\kappa)} + \frac{2\beta\pi \exp(-2\kappa\pi)}{(1 - \exp(-2\kappa\pi))^2} \right] \end{aligned}$$

which leaves the final result. \square

Proof of Theorem 2.2. By using the definition of a circular CDF (see [35]) and (5), we see that

$$\begin{aligned} G(\theta; \kappa, \alpha, \beta) &= \sum_{m=0}^{\infty} F(\theta + 2\pi m; \kappa, \alpha, \beta) - F(2\pi m; \kappa, \alpha, \beta) \\ &= \sum_{m=0}^{\infty} \left(1 - \left(1 + \frac{\kappa\beta(\theta + 2\pi m)}{\alpha\kappa + \beta} \right) \exp(-\kappa(\theta + 2\pi m)) - \left(1 - \left(1 + \frac{\kappa\beta(2\pi m)}{\alpha\kappa + \beta} \right) \exp(-\kappa(2\pi m)) \right) \right) \\ &= \frac{1}{1 - \exp(-2\pi\kappa)} \left(1 - \exp(-\kappa\theta) - \frac{\kappa\beta\theta}{\alpha\kappa + \beta} \exp(-\kappa\theta) \right) + \frac{\exp(-2\pi\kappa)}{(1 - \exp(-2\pi\kappa))^2} \left(\frac{2\pi\kappa\beta}{\alpha\kappa + \beta} \{1 - \exp(-\kappa\theta)\} \right) \end{aligned}$$

which leaves the final result. \square

Proof of Lemma 2.1. By using the definition of the characteristic function and (4), we see that

$$\begin{aligned} \phi_X(t) &= E(\exp(itX)) \\ &= \int_0^{\infty} \exp(itx) \frac{\kappa^2}{\alpha\kappa + \beta} (\alpha + \beta x) \exp(-\kappa x) dx \\ &= \frac{\kappa^2}{\alpha\kappa + \beta} \left[\int_0^{\infty} \alpha \exp(-x(\kappa - it)) dx + \int_0^{\infty} \beta x \exp(-x(\kappa - it)) dx \right] \\ &= \frac{\kappa^2}{\alpha\kappa + \beta} \left[\frac{\alpha(\kappa - it) + \beta}{(\kappa - it)^2} \right]. \end{aligned}$$

which leaves the final result. \square

Proof of Theorem 2.3. By using (6) and the chain rule, we determine the derivative and set it equal to 0:

$$\begin{aligned}
& \frac{d}{d\theta} g(\theta; \kappa, \alpha, \beta) \\
&= \frac{d}{d\theta} \left(\frac{\kappa^2}{\alpha\kappa + \beta} \frac{\exp(-\kappa\theta)}{1 - \exp(-2\pi\kappa)} \left[\alpha + \beta\theta + \frac{2\pi\beta \exp(-2\pi\kappa)}{1 - \exp(-2\pi\kappa)} \right] \right) \\
&= \frac{d}{d\theta} \left(\frac{\alpha\kappa^2}{\alpha\kappa + \beta} \frac{\exp(-\kappa\theta)}{1 - \exp(-2\pi\kappa)} + \frac{\beta\theta\kappa^2}{\alpha\kappa + \beta} \frac{\exp(-\kappa\theta)}{1 - \exp(-2\pi\kappa)} + \frac{\kappa^2}{\alpha\kappa + \beta} \frac{2\pi\beta \exp(-2\pi\kappa)}{1 - \exp(-2\pi\kappa)} \frac{\exp(-\kappa\theta)}{1 - \exp(-2\pi\kappa)} \right) \\
&= \frac{\kappa^2}{(\alpha\kappa + \beta)(1 - \exp(-2\pi\kappa))} \exp(-\kappa\theta) \left(-\alpha\kappa + \beta - \beta\kappa\theta - \frac{2\pi\kappa\beta \exp(-2\pi\kappa)}{1 - \exp(-2\pi\kappa)} \right)
\end{aligned}$$

which implies

$$\underbrace{\exp(-\kappa\theta)}_{=0} \underbrace{\left[-\alpha\kappa + \beta - \beta\kappa\theta - \frac{2\pi\kappa\beta \exp(-2\pi\kappa)}{1 - \exp(-2\pi\kappa)} \right]}_{=0} = 0.$$

Solving for the second bracket leaves the final result.

To confirm that the critical point θ_{mode} in (18) is indeed a maximum, let $C = \frac{\kappa^2}{(\alpha\kappa + \beta)(1 - \exp(-2\pi\kappa))}$ and $A = \frac{2\pi\beta \exp(-2\pi\kappa)}{1 - \exp(-2\pi\kappa)}$ so that

$$\frac{d}{d\theta} g(\theta; \kappa, \alpha, \beta) = C \exp(-\kappa\theta) (\beta - \kappa(\alpha + \beta\theta + A)).$$

From this expression, we note that when we set $\beta - \kappa(\alpha + \beta\theta_{mode} + A) = 0$, we end up with

$$\kappa(\alpha + \beta\theta_{mode} + A) = \beta. \tag{21}$$

Using the chain rule, we find

$$\begin{aligned}
\frac{d^2 g(\theta)}{d^2 \theta} &= \frac{d}{d\theta} (C \exp(-\kappa\theta) (\beta - \kappa(\alpha + \beta\theta + A))) \\
&= -\kappa C \exp(-\kappa\theta) (\beta - \kappa(\alpha + \beta\theta + A)) - \kappa\beta C \exp(-\kappa\theta) \\
&= \kappa C \exp(-\kappa\theta) (\kappa(\alpha + \beta\theta + A) - 2\beta)
\end{aligned}$$

If we evaluate $\frac{d^2 g(\theta)}{d^2 \theta}$ at θ_{mode} (via (21)), we have $\kappa(\alpha + \beta\theta_{mode} + A) - 2\beta = \beta - 2\beta = -\beta$, so that

$$\frac{d^2 g(\theta_{mode})}{d^2 \theta_{mode}} = C \exp(-\kappa\theta_{mode}) \kappa(-\beta) = -\kappa\beta C \exp(-\kappa\theta_{mode}) < 0 \quad \forall \quad \kappa, \alpha, \beta > 0,$$

confirming that the mode is a strict local maximum. \square

A.2 Expressions of (circular) mean, variance, skewness, and kurtosis for the wrapped Lindley distribution (wL) (3) [15]

- Mean direction:

$$\mu = 2 \arctan \left(\frac{1}{\kappa} \right) - \arctan \left(\frac{1}{\kappa + 1} \right);$$

- Circular variance:

$$V_0 = 1 - \frac{\kappa^2}{\kappa + 1} \frac{((\kappa + 1)^2 + 1)^{\frac{1}{2}}}{\kappa^2 + 1};$$

- Circular deviation:

$$\sigma_0 = \sqrt{-2 \log(1 - V_0)} = \sqrt{-2 \log \left(\frac{\kappa^2}{\kappa + 1} \frac{((\kappa + 1)^2 + 1)^{\frac{1}{2}}}{\kappa^2 + 1} \right)};$$

- Coefficient of skewness:

$$\eta_1 = \frac{\bar{b}_2}{V_0^{\frac{3}{2}}}$$

where

$$\begin{aligned} \bar{b}_2 = &= \frac{\kappa^2}{\kappa + 1} \frac{((\kappa + 1)^2 + 4)^{\frac{1}{2}}}{\kappa^2 + 4} \\ &\times \sin \left(2 \arctan \left(\frac{2}{\kappa} \right) - \arctan \left(\frac{2}{\kappa + 1} \right) - 2 \left(2 \arctan \left(\frac{1}{\kappa} \right) - \arctan \left(\frac{1}{\kappa + 1} \right) \right) \right); \end{aligned}$$

and

- Coefficient of kurtosis:

$$\eta_2 = \frac{\bar{a}_2 - (1 - V_0)^4}{V_0^2}$$

where

$$\begin{aligned} \bar{a}_2 = &= \frac{\kappa^2}{\kappa + 1} \frac{((\kappa + 1)^2 + 4)^{\frac{1}{2}}}{\kappa^2 + 4} \\ &\times \cos \left(2 \arctan \left(\frac{2}{\kappa} \right) - \arctan \left(\frac{2}{\kappa + 1} \right) - 2 \left(2 \arctan \left(\frac{1}{\kappa} \right) - \arctan \left(\frac{1}{\kappa + 1} \right) \right) \right). \end{aligned}$$

References

- [1] Nicholas I Fisher and Alan J Lee. Regression models for an angular response. *Biometrics*, pages 665–677, 1992.
- [2] Peter S Petraitis. Occurrence of random and directional movements in the periwinkle, *littorina littorea* (L.). *Journal of Experimental Marine Biology and Ecology*, 59(2-3):207–217, 1982.
- [3] William Bell and Saralees Nadarajah. The wrapped Rama distribution. *Scientific Reports*, 14(1):31936, 2024.
- [4] Abdullah Yilmaz and Cenker Biçer. A new wrapped exponential distribution. *Mathematical Sciences*, 12:285–293, 2018.
- [5] E Zinhom, MM Nassar, SS Radwan, and A Elmasry. The wrapped XLindley distribution. *Environmental and Ecological Statistics*, 30(4):669–686, 2023.
- [6] B Sango Otieno and Christine M Anderson-Cook. Measures of preferred direction for environmental and ecological circular data. *Environmental and Ecological Statistics*, 13:311–324, 2006.
- [7] Lu Chen, Vijay P Singh, Shenglian Guo, Bin Fang, and Pan Liu. A new method for identification of flood seasons using directional statistics. *Hydrological Sciences Journal*, 58(1):28–40, 2013.
- [8] Sahana Bhattacharjee, Inzamal Ahmed, and Kishore Kumar Das. Wrapped two-parameter Lindley distribution for modelling circular data. *Thailand Statistician*, 19(1):81–94, 2021.
- [9] Said Benlakhdar, Mohammed Rziza, and Rachid Oulad Haj Thami. In-depth analysis of von Mises distribution models: Understanding theory, applications, and future directions. *Statistics, Optimization & Information Computing*, 12(4):1210–1230, 2024.
- [10] Sakhr AS Alotaibi, Nora Muda, Ahmad MH Al-Khazaleh, and Shawkat Alkhazaleh. The wrapping Epanechnikov exponential distribution: A novel flexible model for asymmetric circular data. *PLoS One*, 20(9):e0331906, 2025.
- [11] Ahmed M. Gemeay and Ahmed M. T. Abd El-Bar. On wrapping a new version of Lindley distribution for circular data analysis. *Environmental and Ecological Statistics*, 2026.
- [12] William Bell and Saralees Nadarajah. A review of wrapped distributions for circular data. *Mathematics*, 12(16):2440, 2024.
- [13] Nicholas I. Fisher. *Statistical Analysis of Circular Data*. Cambridge University Press, Cambridge, 1995.
- [14] Arthur Pewsey, Markus Neuhäuser, and Graeme D. Ruxton. *Circular Statistics in R*. Oxford University Press, Oxford, 2013.
- [15] Savitri Joshi and KK Jose. Wrapped Lindley distribution. *Communications in Statistics-Theory and Methods*, 47(5):1013–1021, 2018.
- [16] Mohamed E Ghitany, Barbra Atieh, and Saralees Nadarajah. Lindley distribution and its application. *Mathematics and Computers in Simulation*, 78(4):493–506, 2008.
- [17] Rama Shanker, Kamlesh Kumar Shukla, Ravi Shanker, and Tekie Asehun Leonida. A three-parameter Lindley distribution. *American Journal of Mathematics and Statistics*, 7(1):15–26, 2017.
- [18] Rama Shanker, Shambhu Sharma, and Ravi Shanker. A two-parameter Lindley distribution for modeling waiting and survival times data. *Applied Mathematics*, 4(2):363–368, 2013.
- [19] Lars V. Ahlfors. *Complex Analysis*. McGraw-Hill, New York, 3 edition, 1979.
- [20] Gianluca Mastrantonio, Giovanna Jona Lasinio, Antonello Maruotti, and Gianfranco Calise. Invariance properties and statistical inference for circular data. *Statistica Sinica*, 29(1):67–80, 2019.
- [21] Peter J Bickel, Bo Li, Alexandre B Tsybakov, Sara A van de Geer, Bin Yu, Teófilo Valdés, Carlos Rivero, Jianqing Fan, and Aad Van Der Vaart. Regularization in statistics. *Test*, 15(2):271–344, 2006.
- [22] Tin Lok James Ng. Penalized maximum likelihood estimator for mixture of von Mises–Fisher distributions. *Metrika*, 86(2):181–203, 2023.
- [23] Yuejiao Fu, Jiahua Chen, and Pengfei Li. Modified likelihood ratio test for homogeneity in a mixture of von Mises distributions. *Journal of Statistical Planning and Inference*, 138(3):667–681, 2008.
- [24] Luis Rodriguez-Lujan, Pedro Larranaga, and Concha Bielza. Frobenius norm regularization for the multivariate von Mises distribution. *International Journal of Intelligent Systems*, 32(2):153–176, 2017.
- [25] Hirotugu Akaike. A new look at the statistical model identification. *IEEE Transactions on Automatic Control*, 19(6):716–723, 1974.
- [26] Clifford M Hurvich and Chih-Ling Tsai. Regression and time series model selection in small samples. *Biometrika*, 76(2):297–307, 1989.

- [27] Gideon Schwarz. Estimating the dimension of a model. *The Annals of Statistics*, 6(2):461–464, 1978.
- [28] Sreenivasa Rao Jammalamadaka and Tomasz J Kozubowski. New families of wrapped distributions for modeling skew circular data. *Communications in Statistics-Theory and Methods*, 33(9):2059–2074, 2004.
- [29] Jasper Maars, Gijs van Dijk, Mark J Dekkers, F Javier Hernández-Molina, Federico Andreetto, Francisco J Rodríguez-Tovar, and Wout Krijgsman. New palaeocurrent analysis approach from two-dimensional trough cross-strata using photographs and anisotropy of magnetic susceptibility. *The Depositional Record*, 10(2):298–311, 2024.
- [30] AJ Underwood and MG Chapman. Experimental analyses of the influences of topography of the substratum on movements and density of an intertidal snail, *littorina unifasciata*. *Journal of Experimental Marine Biology and Ecology*, 134(3):175–196, 1989.
- [31] Richard J Bolton and David J Hand. Statistical fraud detection: A review. *Statistical Science*, 17(3):235–255, 2002.
- [32] Alejandro Correa Bahnsen, Aleksandar Stojanovic, Djamila Aouada, and Björn Ottersten. Improving credit card fraud detection with calibrated probabilities. In *Proceedings of the 2014 SIAM International Conference on Data Mining*, pages 677–685. SIAM, 2014.
- [33] Mohammed S Eliwa, Emrah Altun, Mohamed El-Dawoody, and Mahmoud El-Morshedy. A new three-parameter discrete distribution with associated INAR(1) process and applications. *IEEE access*, 8:91150–91162, 2020.
- [34] Christophe Ley, Slađana Babić, and Domien Craens. Flexible models for complex data with applications. *Annual Review of Statistics and Its Application*, 8(1):369–391, 2021.
- [35] S. Rao Jammalamadaka and Ambar Sengupta. *Topics in Circular Statistics*. Series on Multivariate Analysis. World Scientific, Singapore, 2001.